Microphysical Enhancement Processes within Stratiform Precipitation on the Barrier and Sub-Barrier Scale of the Olympic Mountains

JOSEPH P. ZAGRODNIK,[a] LYNN MCMURDIE,[b] AND ROBERT CONRICK[b]

[a] *Washington State University, Pullman, Washington*
[b] *University of Washington, Seattle, Washington*

ABSTRACT: High-resolution numerical model simulations of six different cases during the 2015/16 Olympic Mountains Experiment (OLYMPEX) are used to examine dynamic and microphysical precipitation processes on both the full barrier-scale and smaller sub-barrier-scale ridges and valleys. The degree to which stratiform precipitation within midlatitude cyclones is modified over the coastal Olympic Mountains range was found to be strongly dependent on the synoptic environment within a cyclone's prefrontal and warm sectors. In prefrontal sectors, barrier-scale ascent over stably stratified flow resulted in enhanced ice production aloft at the coast and generally upstream of higher terrain. At low levels, stable flow orientated transverse to sub-barrier-scale windward ridges generated small-scale mountain waves, which failed to produce enough cloud water to appreciably enhance precipitation on the scale of the windward ridges. In moist-neutral warm sectors, the upstream side of the barrier exhibited broad ascent oriented along the windward ridges with lesser regions of adjacent downward motion. Significant quantities of cloud water were produced over coastal foothills with further production of cloud water on the lower-windward slopes. Ice production above the melting layer occurred directly over the barrier where the ice particles were further advected downstream by cross-barrier winds and spilled over into the lee. The coastal foothills were found to be essential for the production and maintenance of cloud water upstream of the primary topographic barrier, allowing additional time for hydrometeors to grow to precipitation size by autoconversion and collection before falling out on the lower-windward slopes.

KEYWORDS: Extratropical cyclones; Precipitation; Cloud microphysics; Aircraft observations; Mesoscale models; Mountain meteorology

1. Introduction

As midlatitude cyclones approach mountain ranges on the west coasts of continents, their precipitating structures are modified by changes to the three-dimensional flow field occurring on the scale of the barrier as a whole and localized perturbations over smaller-scale ridges and valleys. Barrier-scale mechanisms may include an upstream shift in precipitation enhancement during blocked flow regimes (Houze et al. 2001; James and Houze 2005) or deep barrier-scale enhancement up to a height of 8 km during unblocked regimes (McMurdie et al. 2018). Sub-barrier-scale processes may include melting and/or evaporation-induced down-valley flow (Steiner et al. 2003; Asencio and Stein 2006; Thériault et al. 2012), shear-induced turbulent layers (Medina et al. 2005, 2007), and small-scale mountain waves over windward ridges (Garvert et al. 2007; Minder et al. 2008). In many cases, patterns of precipitation over complex terrain can be approximated by a steady-state mountain wave response to a uniform, moist, and stably stratified upstream flow (Smith and Barstad 2004). Reasonable patterns of ridge–valley precipitation enhancement can be achieved by parameterizing time scales of

microphysical growth, particle fallout, and advection (Anders et al. 2007). To achieve observed enhancement rates, condensate must be converted to precipitation and reach the surface before it is advected over the ridge or evaporates on the lee side.

Accelerated microphysical processes are especially important on smaller-scale ridges where any condensate formed by ascent on the windward side has a short amount of time to reach precipitation size and fall out. Many studies have observed or modeled processes resembling the "seeder–feeder" effect (Bergeron 1968), which refers to the enhancement of precipitation on a small ridge when condensate falling from a preexisting higher cloud collects cloud drops from a separate, lower-level cloud, resulting in a more efficient precipitating cloud. Most of the canonical seeder–feeder experiments were conducted during frontal cyclone passages over the Glamorgan Hills region of south Wales, United Kingdom. (Browning et al. 1974; Hill et al. 1981; Richard et al. 1987), a region of numerous small coastal hills with a maximum elevation of 600 m. Under these conditions, it was determined that precipitation enhancement was often significant and concentrated in radar observations over the lowest 1.5 km above terrain (Hill et al. 1981). Atmospheric conditions favoring enhanced precipitation over terrain included warm sectors with low-level jets of at least $20 \, \mathrm{m \, s^{-1}}$ (i.e., atmospheric rivers) and upwind "seeder" precipitation of at least $0.5 \, \mathrm{mm \, h^{-1}}$ (Nash and Browning 1977; Hill et al. 1981; Richard et al. 1987).

A commonly held assumption of the seeder–feeder framework is that the lower-level warm processes are inefficient

---

because of slow autoconversion rates between cloud and rainwater. Several studies over the coastal California mountains and coastal Chilean mountains (White et al. 2003; Kingsmill et al. 2006; Martner et al. 2008; Massmann et al. 2017) used the presence of a bright band in vertically profiling radar to separate periods of exclusively warm (nonbrightband) rain from periods when ice-generated particles might be collecting cloud or rainwater. Surprisingly, the warm rain periods, characterized by large concentrations of small raindrops, were found to produce rain rates up to $20\,\mathrm{mm\,h^{-1}}$ (White et al. 2003). While periods containing bright bands did have higher rain rates overall, these studies demonstrated that the traditional seeder–feeder interpretation was not necessary to appreciably enhance precipitation under certain conditions.

More recent studies have resulted in an increasingly complicated model of how seeder–feeder processes may occur. In a study over a ~1-km height windward ridge of the Olympic Mountains, Minder et al. (2008) found robust patterns of finescale precipitation enhancement associated with ridge-induced mountain waves. A model simulation of a particularly intense storm showed that collection of cloud water by rain was the dominant conversion term, but there was "no clear separation between synoptically forced clouds and orographically forced clouds, both of which seed and feed the collection process." (Minder et al. 2008). Importantly, collection terms from a bulk microphysical scheme cannot be used to directly diagnose the seeder–feeder mechanism, as the initial source of the "seed" doing the collecting may have originated from the preexisting nimbostratus cloud associated with the frontal cyclone, the orographic "feeder" cloud, or both. To further complicate matters, several studies have demonstrated that larger mountain ranges are capable of enhancing ice processes on the scale of the barrier throughout the depth of the larger-scale stratiform cloud (Kingsmill et al. 2006; Medina et al. 2007; McMurdie et al. 2018), providing an additional source of ice-initiated hydrometeors that may accelerate the collection of cloud water at lower levels.

The 2015/16 Olympic Mountains Experiment (OLYMPEX; Houze et al. 2017), deployed numerous radars, rain gauges, and disdrometers at a large number of ground sites on the windward side of the Olympic Mountains in Washington State. Purnell and Kirshbaum (2018) used a combination of OLYMPEX observations and quasi-idealized numerical experiments to determine the sensitivity of precipitation enhancement to various upstream parameters associated with the passage of different frontal cyclone sectors. To test the role of the seeder–feeder process, they simulated an idealized warm sector with a uniform sounding and parameterized large-scale forcing over the realistic Olympic Mountains terrain. Similar to Richard et al. (1987), they found that windward precipitation efficiency in both warm frontal and warm sector simulations was greatly improved by including a small amount (up to $0.5\,\mathrm{mm\,h^{-1}}$) of upstream precipitation (i.e., the preexisting "seeder" precipitation that impinges upon the mountain).

A pair of complementary OLYMPEX observational studies (Zagrodnik et al. 2018, 2019) found patterns of precipitation enhancement matching Purnell and Kirshbaum (2018) in different midlatitude storm sectors, with the added benefit of

surface particle size distribution (PSD) observations to gain insight into the dominant microphysical enhancement processes leading to the observed precipitation patterns. While prefrontal (also known as warm frontal or prewarm frontal) periods had relatively invariant PSDs indicative of ice-generated stratiform rain, warm sectors contained remarkable variability in droplet size and number concentration. Large concentrations of small drops were often observed in association with significant precipitation enhancement at lower-windward elevations (i.e., below 1000 m including ridges and valleys), especially during strongly forced warm sector periods containing environmental conditions favorable for warm rain processes. The precipitation rate on the lower-windward slopes was remarkably steady during a warm sector case study despite variations in the drop size distribution caused by the passage of a deeper feature that temporarily enhanced ice processes. During periods of intense rainfall, periods with high concentrations of small drops were presumably a result of autoconversion and self-collection within the liquid cloud layer (i.e., warm rain), rather than collection by "seeder" raindrops, which was believed to be more prominent in the periods with larger median drop sizes (Zagrodnik et al. 2018).

The contrasting results in the above studies leave significant open questions about the relative roles of warm and ice precipitation processes in enhancing precipitation on coastal mountain ranges. OLYMPEX studies (Zagrodnik et al. 2018; McMurdie et al. 2018; Purnell and Kirshbaum 2018, Zagrodnik et al. 2019) agree on the importance of the upstream environment for enhancing precipitation in warm sector periods characterized by moist-neutral onshore flow, high melting levels, and high quantities of horizontal vapor transport. In prefrontal periods containing a stably stratified environment, low melting levels, and an offshore component to the low-level wind, warm processes are nearly absent and precipitation enhancement is modest. However, the OLYMPEX observational network was not designed to observe localized variability over small-scale ridges (Minder et al. 2008), and the semi-idealized nature of the simulations in Purnell and Kirshbaum (2018) makes it difficult to directly compare with Zagrodnik et al. (2018, 2019).

By examining microphysical output from realistic Weather Research and Forecasting (WRF) simulations, this study evaluates the relative importance of warm and cold precipitation processes on the full barrier scale as well as on localized sub-barrier ridges and valleys. The model setup, evaluation, and verification are guided by the OLYMPEX observations detailed in Zagrodnik et al. (2019). Model runs from several prefrontal and warm sector cases are used to determine the key processes of enhancement on different spatial scales. Additionally, a simple terrain-modification experiment is conducted to evaluate the role of the coastal foothills in windward precipitation enhancement in warm sectors. More broadly, this study aims to augment observational and modeling studies over the Olympic Mountains to provide a more complete understanding of the dynamic and microphysical processes responsible for enhancing precipitation over midlatitude mountain ranges on the west coasts of continents.
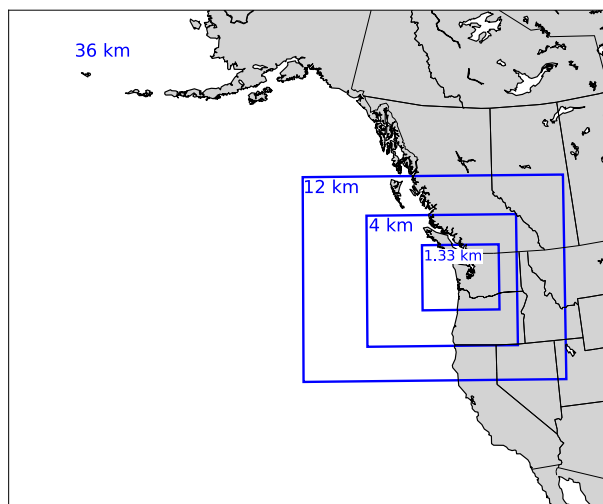
FIG. 1. Map of the nested WRF-ARW domains used in this study. Labels indicate the resolution of the four domains.

2. Data and methods

a. Model configuration

The simulations examined in this study were conducted using the Advanced Research version of the Weather Research and Forecasting Model (WRF-ARW; Skamarock et al. 2008) version 3.8.1. The model setup was similar to previous OLYMPEX studies that were found agree with synoptic observations, although the model is prone to underpredicting cloud water and overpredicting snow mixing ratios (Conrick and Mass 2019a; Conrick and Mass 2019b). Figure 1 shows the 36–12–4–1.33-km model domain configuration with 51 vertical levels. The innermost 1.33-km domain is centered over the Olympic Peninsula. Model initialization and boundary conditions were driven by the 0.25° Global Forecast System (GFS) gridded dataset. The 36-km grid boundaries were nudged every 3 h using either the GFS initialization (0000, 0600, 1200, and 1800 UTC) or the 3-h forecast (0300, 0900, 1500, and 2100 UTC). Table 1 contains additional model parameterization selections. The cumulus scheme (Grell–Freitas; Grell and Freitas 2014) is not used on the innermost domain. The most noteworthy parameterization choice is the use of the Thompson microphysics scheme (Thompson et al. 2008), which was chosen because of its long history of use in the Pacific Northwest as well as a demonstrated ability to more accurately predict liquid water content (LWC) during OLYMPEX than other microphysics schemes (Conrick and Mass 2019b).

b. Case selection and model validation

This study uses cases from the same set of NASA DC-8 aircraft missions (Durden and Tanelli 2018) detailed in Zagrodnik et al. (2019). Table 2 shows the cases, model initialization times, and model analysis times for the six cases in this study. Three prefrontal and three warm sector cases are considered. The 3 December case was sampled for a shorter period than the other cases and is therefore slightly underrepresented in the analysis relative to the other cases in this

TABLE 1. WRF parameterization choices used in this study.

Parameterization	Configuration	Reference
Microphysics	Thompson	Thompson et al. (2008)
Land surface	Noah-MP	Niu et al. (2011)
Radiative transfer	RRTMG	Iacono et al. (2008)
Cumulus	Grell–Freitas	Grell and Freitas (2014)
Boundary layer	Yonsei University	Hong et al. (2006)

study. The storm sector paradigm and the rationale for examining the sectors separately is described in Medina et al. (2007) and Zagrodnik et al. (2018). Postfrontal cases were poorly resolved by the model and are not included. The analysis start and end times were set according to the OLYMPEX DC-8 flight times, each of which sampled for ~2–5 h, usually in a "race track" pattern of repeated SW–NE transects of the Olympic Mountains. The flight pattern was designed to repeatedly pass over a dense network of surface radars, rain gauges, and disdrometers that were mostly positioned along a SW–NE line from the coast into the Quinault Valley, which is outlined in Fig. 2. The WRF model output was saved every hour and output from the 1.33-km domain was composited to generate contoured frequency by altitude diagrams (CFADs) of simulated radar reflectivity and maps of various dynamic and microphysical parameters.

Model kinematic and thermodynamic output was validated by comparing soundings launched at the OLYMPEX coastal radar site (Fig. 2) with interpolated WRF soundings at the timestamp nearest to the sounding launch. Two important parameters for microphysical interpretation, integrated vapor transport (IVT) and melting level are compared in Table 3. The observations and model differed by 5% on average with a maximum departure of 11%. These departures are well within an acceptable range, especially since sounding drift and time differences were not considered.

3. Model evaluation using aircraft and surface observations

a. Reflectivity CFADs

Before evaluating model microphysical output, it is important to verify that the model is producing precipitation structures that are consistent with observations. In Zagrodnik et al. (2019), CFADs of radar reflectivity from the attenuation-corrected Ku-band channel of the Airborne Precipitation and Cloud Radar Third Generation (APR-3) were created by dividing the flight legs into five geographic regions: ocean, coast, windward, high terrain, and lee side. Figure 2 shows the corresponding ocean and windward geographic regions used to partition the WRF CFADs. Using WRF for diagnostic purposes gives the advantage of uniform sampling at 1.33-km horizontal resolution over the full ocean and windward sectors instead of being preferentially biased along the typical DC-8 flight pattern, shown as lines in Fig. 2. To allow quantitative comparison between the APR-3 and WRF, the WRF CFADs were constructed as in Zagrodnik et al. (2019) with the same bin spacing (1-dB reflectivity and 0.25-km height intervals) and

TABLE 2. Cases, model initialization times, and model analysis times used in this study.

Case	Category	WRF initialization time	Analysis start	Analysis end	No. of WRF hourly time steps used
1 Dec 2015	Prefrontal	1200 UTC 1 Dec	2100 UTC 1 Dec	0200 UTC 2 Dec	6
5 Dec 2015	Prefrontal	0000 UTC 3 Dec	1400 UTC	1900 UTC	6
12 Dec 2015	Prefrontal	0000 UTC 12 Dec	1600 UTC	2200 UTC	7
13 Nov 2015	Warm sector	1200 UTC 12 Nov	1400 UTC	2000 UTC	7
3 Dec 2015	Warm sector	0000 UTC 3 Dec	1400 UTC	1700 UTC	4
8 Dec 2015	Warm sector	0000 UTC 8 Dec	1300 UTC	1900 UTC	7

normalization by overall maximum bin. Reflectivity in WRF is derived from the drop size distribution of the microphysical output assuming a 10-cm (S-band) wavelength radar with appropriate corrections for ice particles and water-coated ice particles. The gray shaded terrain in Fig. 2 also illustrates the pattern of smaller, sub-barrier-scale ridges and valleys that are superimposed on the broader barrier-scale dome shape of the Olympic Mountains.

Figure 3 shows a comparison between the APR-3 and WRF CFADs for the windward region only. Similar results were obtained for the ocean region (not pictured). The APR-3 panels (Fig. 3, top row) are reproduced from Zagrodnik et al. (2019) Figs. 7d and 13d. Many of the key features in the observations are reproduced by the model (Fig. 3, bottom row). Both prefrontal CFADs show a narrow range of reflectivities corresponding to homogeneous stratiform precipitation. However, simulated reflectivity is overestimated by 5–10 dB, especially in the ice layer, a behavior that was also noted in atmospheric river-type storms in California (Jankov et al. 2009). The observed and simulated warm sector CFADs are both broader than the prefrontal sector, although the WRF CFAD is smoother as a consequence of the larger sample size and lower vertical resolution. The WRF CFAD also locates the warm sector mode centered near 3–4-km altitude, a reflection of low- to midlevel enhancement of precipitation. The observations also suggest stronger below-brightband (e.g., below 2.5 km; the average warm sector melting level height) precipitation than the simulated reflectivity suggests, an indication that WRF is identifying but underestimating low-level warm processes.

Figure 4 examines the nature of windward precipitation enhancement by taking the CFAD difference between the windward side (Fig. 3) and the ocean (not pictured). The APR-3 panels (Fig. 4, top row) are reproduced from Zagrodnik et al. (2019) Figs. 8b and 14b. WRF captures the area of midlevel reflectivity enhancement in both prefrontal and warm sectors, although it is somewhat underestimated in prefrontal sectors. The greatest disagreement is the lack of WRF low-level enhancement in warm sectors near and below the melting level. In general, the qualitative agreement in reflectivity structures between WRF and observation is quite impressive given the complexity of terrain-induced enhancement processes.

b. Surface precipitation rate

Figure 5 shows both the average WRF surface precipitation rate and observed precipitation rate in the prefrontal and warm sector cases during the hours detailed in Table 2. Precipitation

observations were obtained from both OLYMPEX sites (Petersen et al. 2017a,b) and the MesoWest archive (Horel et al. 2002). WRF correctly resolves the major differences in precipitation patterns between prefrontal and warm sectors. Prefrontal precipitation rates are generally light, $<5\,\mathrm{mm\,h^{-1}}$, with slight enhancement over the coast and windward side. Warm sectors have lighter precipitation rates at the coast than the prefrontal sector and a rapid increase to $>10\,\mathrm{mm\,h^{-1}}$ rain rates over the windward ridges and southwestern part of the high terrain. Leeside precipitation rates are greater in the warm sector than the prefrontal sector. Finescale ridge–valley gradients in precipitation rate on the windward site are most pronounced during warm sectors. Notably, observations on ridges were sparser than at lower elevations. The major precipitation patterns in the WRF simulations also compare favorably with the more sophisticated gauge-radar precipitation retrieval shown in Purnell and Kirshbaum (2018) Figs. 7a and 7b, which included a larger sample size of prefrontal and warm sector cases.
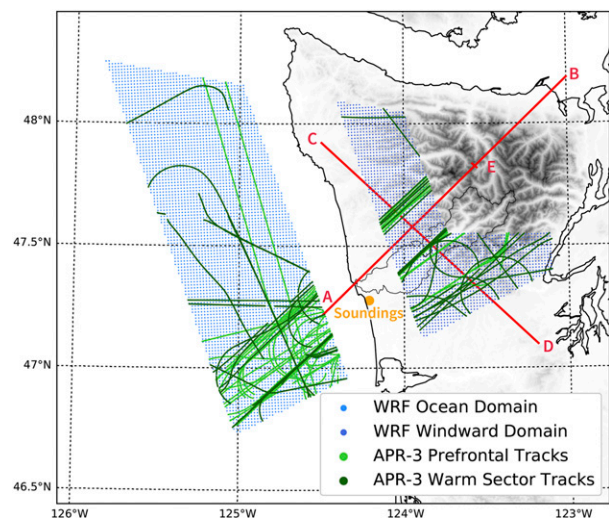

FIG. 2. Map of the ocean and windward geographic regions used to generate the CFADs in Figs. 3 and 4. Color shaded areas denote the ocean (light blue) and windward (dark blue) domains used in the WRF CFADs. Lines denote the prefrontal (light green) and warm sector (dark green) DC-8 flight paths used in the APR-3 CFADs. The orange dot denotes the sounding launch location (Table 3). The red lines denote the cross section in Figs. 8, 9 and 10. Darker gray shades over land denote higher terrain. The black outline over land denotes the Quinault River basin, which includes the Quinault valley.

TABLE 3. Comparison of integrated vapor transport (IVT) and melting level between soundings launched at the coast (location in Fig. 2) and WRF output interpolated to the launch location.

Case	Sounding launch (UTC)	WRF time (UTC)	Observed IVT $(kg\,m^{-1}\,s^{-1})$	WRF IVT $(kg\,m^{-1}\,s^{-1})$	Observed melting level (m)	WRF melting level (m)
1–2 Dec 2015	2317	2300	500	441	2103	2053
5 Dec 2015	1514	1500	560	582	2031	1974
12 Dec 2015	1914	1900	529	485	879	884
13 Nov 2015	1632	1700	575	621	2538	2553
3 Dec 2015	1516	1500	784	807	2150	2324
8 Dec 2015	1515	1500	815	856	2769	2847

Comparing the gridded model output to the point observations reveals a few general trends that are relevant for interpreting the WRF output in the rest of this study. In prefrontal sectors, WRF is visually very close to observations, although direct comparisons (not pictured) suggest slight overestimation by WRF over terrain, possibly due to the excessive ice production noted in the CFADs (Fig. 4). In warm sectors, WRF differed from gauge observations by up to $\pm 3\,mm\,h^{-1}$ at a few low- to mid-elevation windward sites on the southern side of the Olympic Mountains. Even small differences in precipitation rate can become significant when considering the long duration of these storm systems. The source of these disagreements is uncertain but possibly related to the model having difficulty resolving the complexity and greater intensity of terrain-enhanced warm sector precipitation. While the details may differ, the overall, qualitative consistency of WRF-observation CFADs and precipitation patterns adds confidence that WRF dynamical and microphysical fields described in the following sections are generally representative of the dominant precipitation processes within these storms.

4. Synoptic and dynamical composites

a. Flow and stability

Figure 6 shows model composite surface and 500-hPa maps and Figs. 7a and 7b shows model composite low-level moist static stability (N_m^2). All model composites in this study are generated by averaging the hourly WRF output for the time periods for each case listed in Table 2. The moist static stability was calculated by determining N_m^2 following Durran and Klemp (1982) over interpolated vertical layers at 0.25-km spacing and averaging over the 0.5–2.0-km layer. Consistent with previous OLYMPEX studies (Zagrodnik et al. 2018; Zagrodnik et al. 2019), we use N_m^2 to indicate if flow is likely to ascend over the dome-shaped Olympic Mountains or be prone to low-level blocking or deflection upstream of the barrier.

The 500-hPa composites (Figs. 6a,b) show that the average cross-barrier flow was from the west-southwest during both prefrontal and warm sector periods. The composites obscure some case-to-case variability, for example the 3 December 2015 case was more southerly than the other warm sector cases (Zagrodnik et al. 2019). The 500-hPa flow speed over terrain was slightly stronger (5–10 kt; 1 kt $\approx$ $0.51\,m\,s^{-1}$) in warm sectors and the heights were lower on

average in prefrontal sectors. Composite flow at 700 hPa (not pictured) was also from the west-southwest, while 850-hPa flow (not pictured) was southerly near the Olympic Mountains in prefrontal sectors and southwesterly in warm sectors. The composite surface maps (Figs. 6c,d) show more significant differences between the two sectors. Prefrontal sectors had more southerly flow with an offshore-directed pressure gradient at the coast. There was also strong evidence of flow deflection on the south and southwest sides of the Olympic Mountains where the 10-m winds were east to southeasterly. Warm sectors had isobars roughly perpendicular to the coast and southwesterly 10-m winds at the coast and over the windward slopes. There was only a slight indication of flow deflection in surface flow directly upstream of the barrier over land.

Composite 0.5–2.0-km moist static stability (N_m^2, Fig. 7a) shows stably stratified low levels upstream of the Olympic Mountains in the prefrontal sector, especially over land. Similar to the 10-m flow, the 925-hPa flow shows indications of deflection around the barrier on the southwest side corresponding to the region of greatest stable stratification. Warm sectors (Fig. 7b) were closer to moist-neutral as N_m^2 was between 0 and $0.25 \times 10^{-4}\,s^{-2}$ upstream of the Olympic Mountains. The 925-hPa flow was nearly uniform from the southwest with no indication of flow deflection on the windward side.

b. Vertical velocity and relative humidity

Given the considerable differences in low-level flow and stability between different storm sector composites detailed in the previous section, it is expected that regions of ascent and descent will differ in location and magnitude between prefrontal and warm sectors. Figures 7c and 7d shows a map of the composite average vertical velocity in the lowest 2.0 km above terrain. Cross sections of the composite vertical velocity are shown in Figs. 8a and 9 for prefrontal and Fig. 10a for warm sectors. The SW–NE cross section (Fig. 8a) is oriented along the midlevel flow (A–B in Fig. 2) and the NW–SE cross section (Fig. 9) is orientated along the lower-level flow (C–D in Fig. 2). On windward ridges, prefrontal sectors had pronounced couplets of ascent and descent over the smaller windward ridges. These waves are most pronounced in stably stratified layer below ~3 km where a greater potential temperature gradient was present. The presence of a critical layer associated with the wind veering to the southwest (Figs. 6a,c and 9) likely reduces further upward propagation.
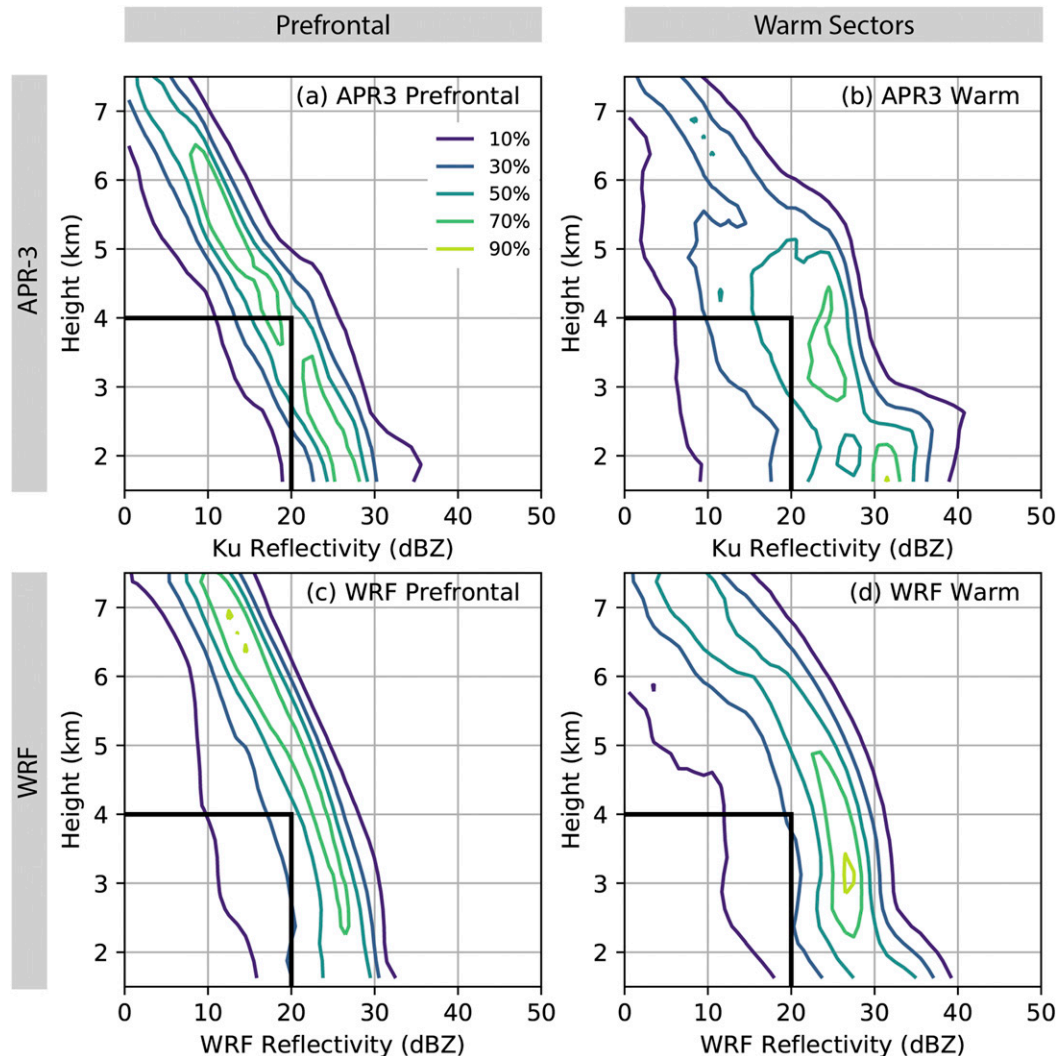
FIG. 3. Normalized contoured frequency by altitude diagrams (CFADs) for the windward region (a) APR-3 prefrontal cases, (b) APR-3 warm sector cases, (c) WRF prefrontal cases, and (d) WRF warm sector cases. (a),(b) Reproduced from Zagrodnik et al. (2019). A solid black line at 4 km and 20 dBZ is included for easier comparison between panels.

In the map (Fig. 7c) and SW–NE cross section (Fig. 9), a second set of high-amplitude, vertically propagating mountain waves is apparent over the high terrain with lee waves extending downstream of terrain. These waves were aligned with the cross-barrier midlevel flow, perpendicular to the waves over the windward ridges. Overall, this wave pattern is similar to the waves over the Oregon Cascades detailed in Fig. 19 of Garvert et al. (2007) and the Olympic Mountains in Minder et al. (2008). Examination of each model time step (not shown) revealed that this stationary wave pattern was observed throughout the three prefrontal cases with only minor variations.

Warm sector vertical velocities (Figs. 7d and 10a) also show small-scale waves associated with ridges on the windward side extending up to 3-km height, but in this case they are aligned along the SW–NE corridor, parallel to the primary windward

ridge. However, smaller topographic perturbations perpendicular to the southwesterly flow (Fig. 2) are still enough to generate small-scale waves with an associated microphysical response that is described in section 5. Compared with prefrontal sectors, warm sectors were characterized by broader ascent across the windward ridges with smaller corresponding regions of descent (Fig. 7d). The model also shows enhanced ascent over the coastal foothills, from 0 to 25 km horizontally along the cross section (Fig. 10a). Evaluation of individual cases (not pictured) confirms that the prefrontal and warm sector differences were robust. In warm sectors, the moist-neutral upstream environment supported broad lifting over the barrier. The low-level flow was aligned along the windward ridges (SW to NE) rather than normal to the ridges, further reducing regions of descent. The high-amplitude wave response over the high terrain–lee side was similar in structure
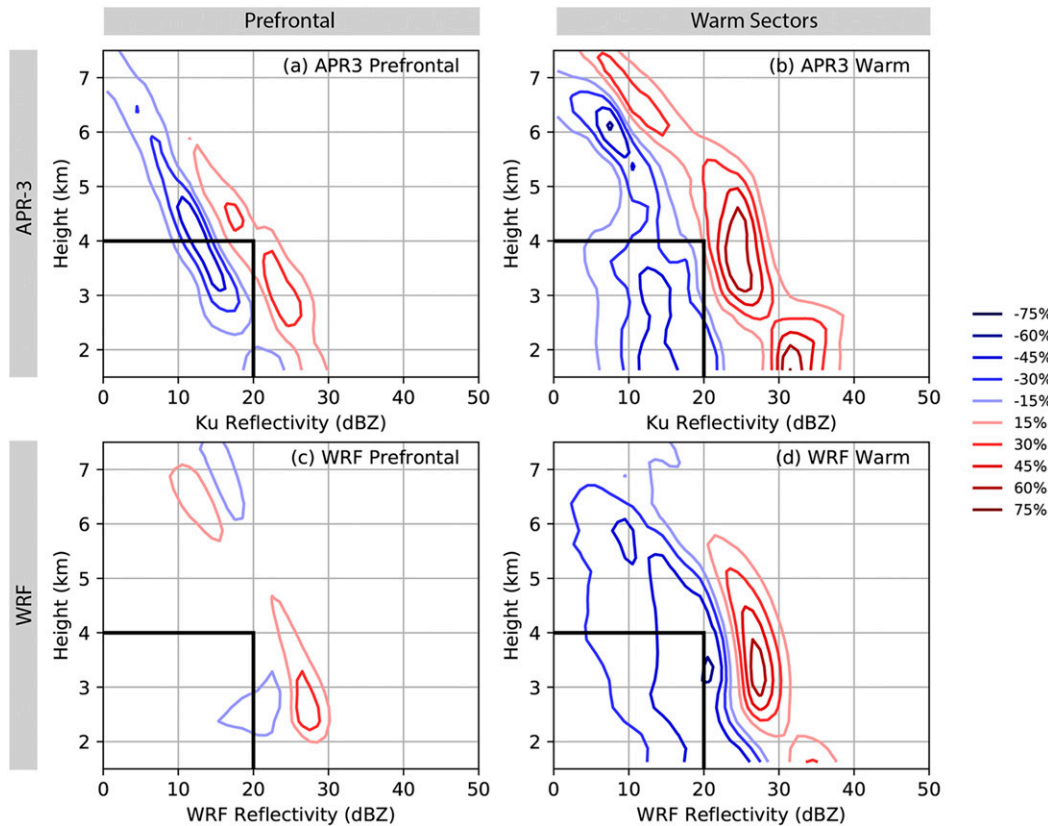
FIG. 4. Difference CFADs computed by subtracting the ocean region from the windward region for (a) APR-3 prefrontal cases, (b) APR-3 warm sector cases, (c) WRF prefrontal cases, and (d) WRF warm sector cases. (a),(b) Reproduced from Zagrodnik et al. (2019).

and greater in magnitude than prefrontal sectors, consistent with the similar direction and stability, plus slightly stronger velocity of the midlevel cross-barrier flow in Fig. 6b.

Figures 7e and 7f shows the composite WRF relative humidity (RH) over the lowest 1.0 km above the terrain. With widespread precipitation ongoing, the low levels upstream of the barrier tended to be nearly saturated (>95% RH) in both prefrontal and warm sectors. Prefrontal sectors had a pattern of saturation and drying on the smaller-scale windward ridges that correspond with the regions of ascent and descent in
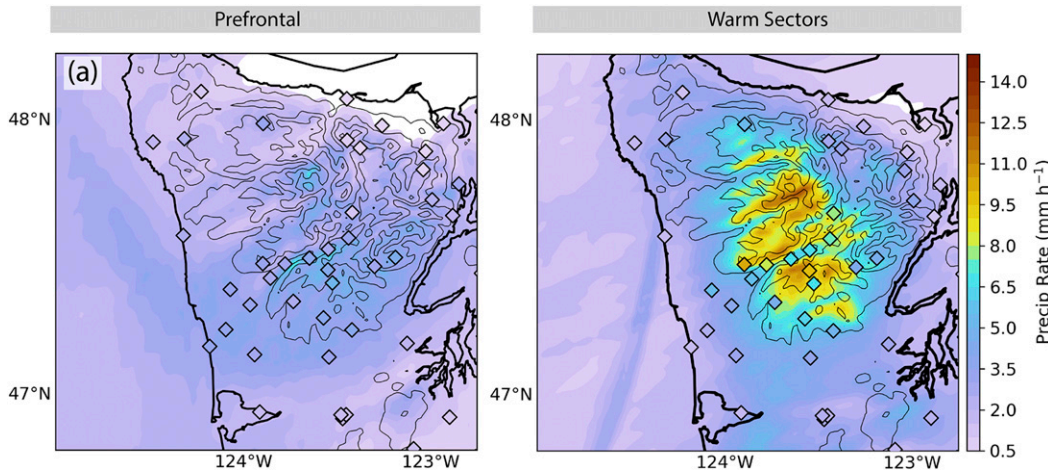
FIG. 5. Average WRF surface precipitation rate (shaded contours; mm h^{-1}) and observed precipitation rate (shaded diamonds) in (a) prefrontal and (b) warm sector events.
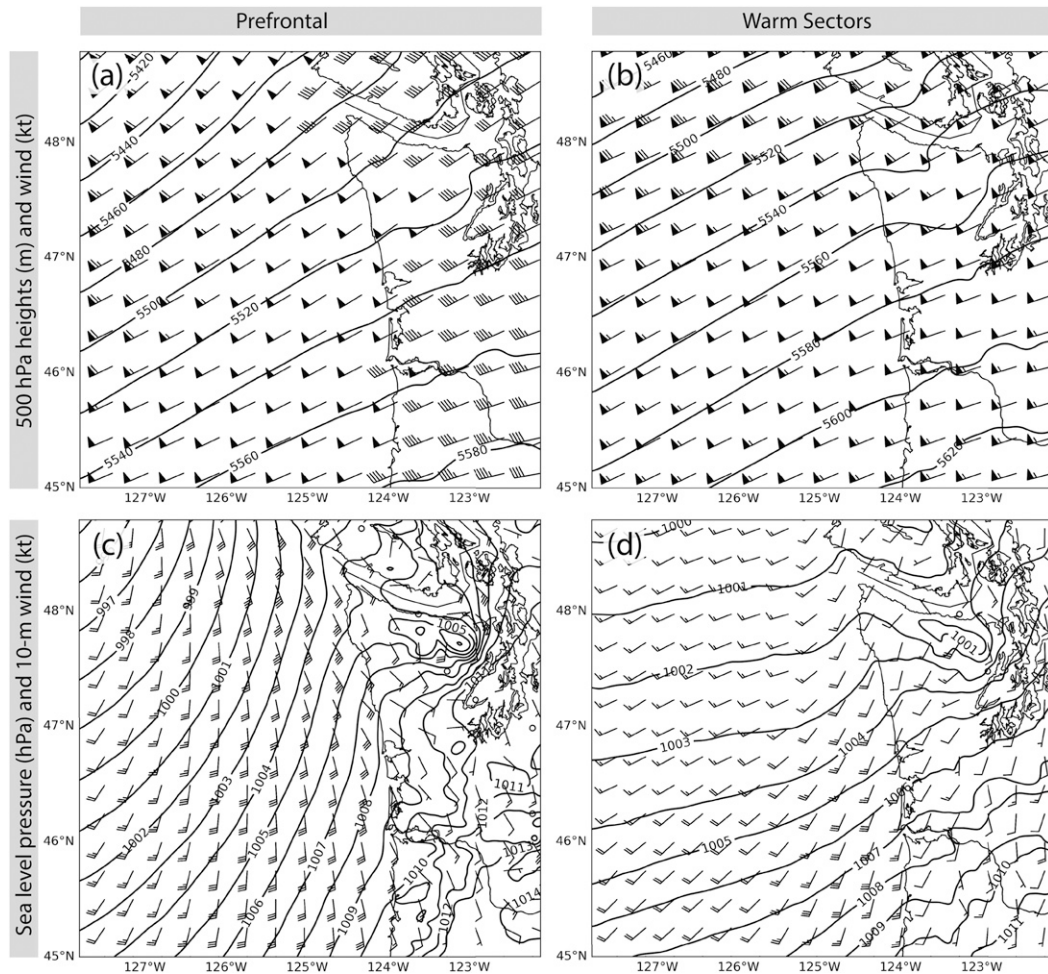
FIG. 6. (top) Composite WRF 500-hPa height (m; contours) and wind (kt; barbs) for (a) prefrontal and (b) warm sectors. (bottom) Composite WRF sea level pressure (hPa; contours) and 10-m wind (kt; barbs) for (c) prefrontal and (d) warm sectors.

Figs. 7c, 8a and 9. Areas of near 100% RH were confined to the ridges. In contrast, warm sectors were essentially saturated everywhere on the coast and windward slopes, except for a few isolated pockets such as the interior Quinault Valley. In the next section, we demonstrate that these profound differences in low-level vertical motions and moisture have major implications for the microphysical precipitation processes in these regions.

5. Microphysical composites

Figures 8b–d and 10b–d show SW–NE composite cross sections of the average cloud water + cloud ice mixing ratio (Figs. 11a,b), average rainwater mixing ratio (Figs. 11c,d), and average frozen hydrometeor (graupel + snow) mixing ratio. Corresponding map composites using vertically averaged mixing ratios are shown in Fig. 11. The pattern of small-scale mountain waves in the prefrontal sector (Figs. 7b, 8a and 9) appears to have been responsible for only a minor increase in cloud water on windward ridges (Figs. 8b and 11a). The regions of descent

and drying on the lee of windward ridges were responsible for local reductions in cloud water, but no progressive increase in precipitation as flow moves over successive ridges. In prefrontal sectors there is almost no visible increase in rain or frozen hydrometeor mixing ratios on the scale of individual windward ridges (Figs. 8b,c and 11c,d). Instead, the prefrontal frozen hydrometeor mixing ratio (Figs. 8d and 11e) was broadly elevated on the southern side of the Olympic Mountains and somewhat over the center of the barrier. The lack of localized increases in mixing ratios suggests that barrier-scale lift was controlling the precipitation enhancement in these prefrontal cases. The greatest frozen hydrometeor mixing ratios (Figs. 8d and 10e) were displaced upstream of the high terrain, likely a consequence of broader ascent over low-level stable air (Fig. 7, Houze et al. 2001; James and Houze 2005). A second area of elevated frozen hydrometeor mixing ratios can be clearly seen near the center of the Olympic Mountains (Fig. 8d), in association with a larger region of ascent between the windward ridges and the high terrain (Fig. 8a). Precipitation rates were broadly enhanced over the windward slopes as a consequence
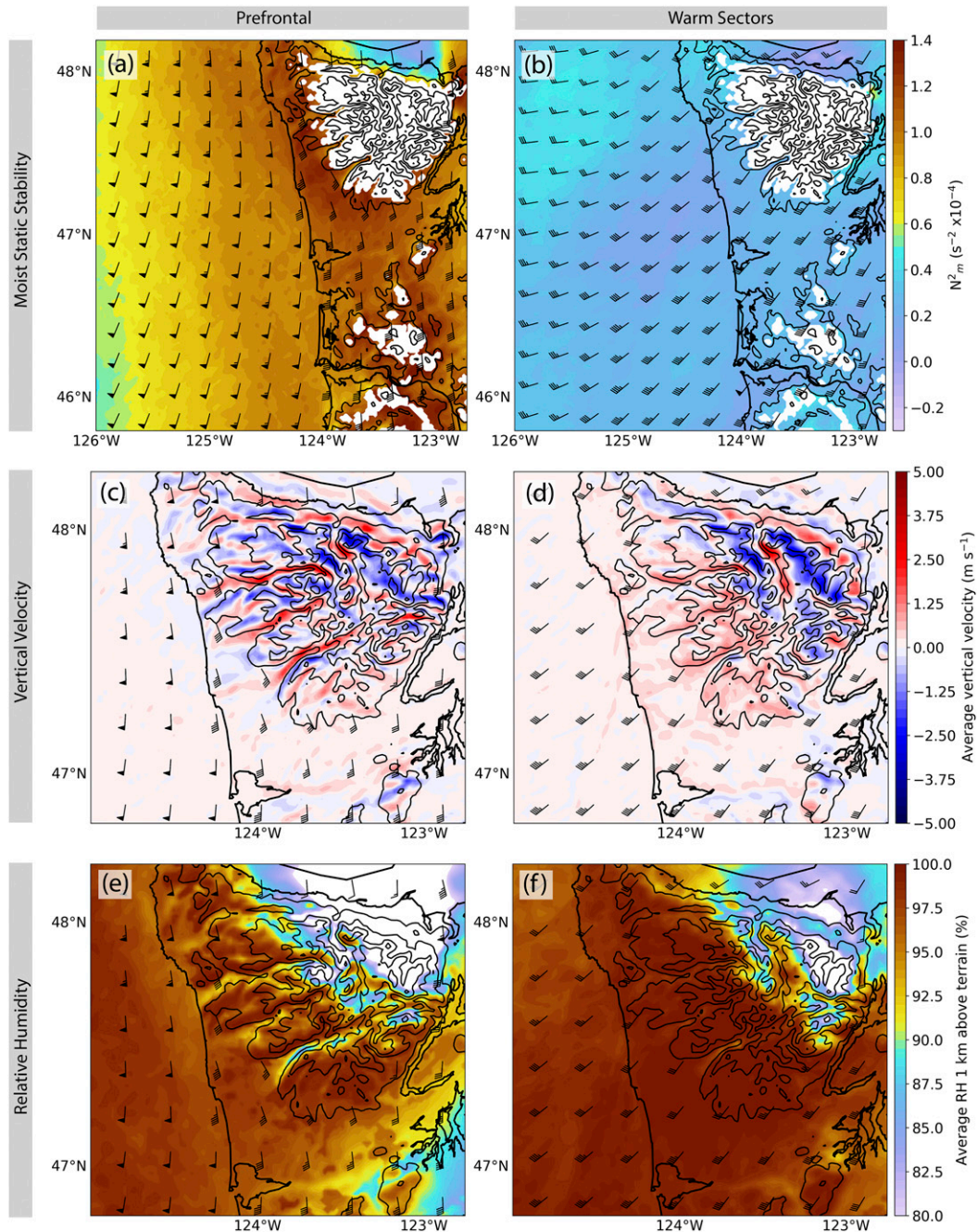
FIG. 7. Composite WRF maps of (a),(b) 0.5–2.0-km moist static stability ($N_m^2 \times 10^{-4}$; contours) and 925-hPa wind (kt; barbs); (c),(d) vertical velocity (m s^{-1}) averaged in the 0–2.0-km layer above the terrain and 925-hPa wind (kt; barbs); and (e),(f) relative humidity (%) averaged in the 1.0-km layer above the terrain and 925-hPa wind (kt; barbs). Prefrontal composites are in (a), (c), and (e) and warm sector composites are in (b), (d), and (f).

of these ice-dominated processes (Fig. 5a) with a minimal contribution from processes over localized small-scale ridges. Hydrometeor drift caused by 40–50-kt cross-ridge winds (Fig. 8d) may have also aided in smoothing out any differences in rain between small-scale ridges and subsequent valleys (Minder et al. 2008).

The distribution of cloud water was markedly different in warm sectors (Figs. 10b and 11b). The greatest cloud

water enhancement was located on the upstream side of all major windward ridges, but cloud water was also elevated at lower elevations at the mouth of windward valleys (except in the interior Quinault valley). Additionally, enhanced cloud water was widespread over the coastal foothills upstream of the main barrier. The quantity of cloud water produced was impressive given that the
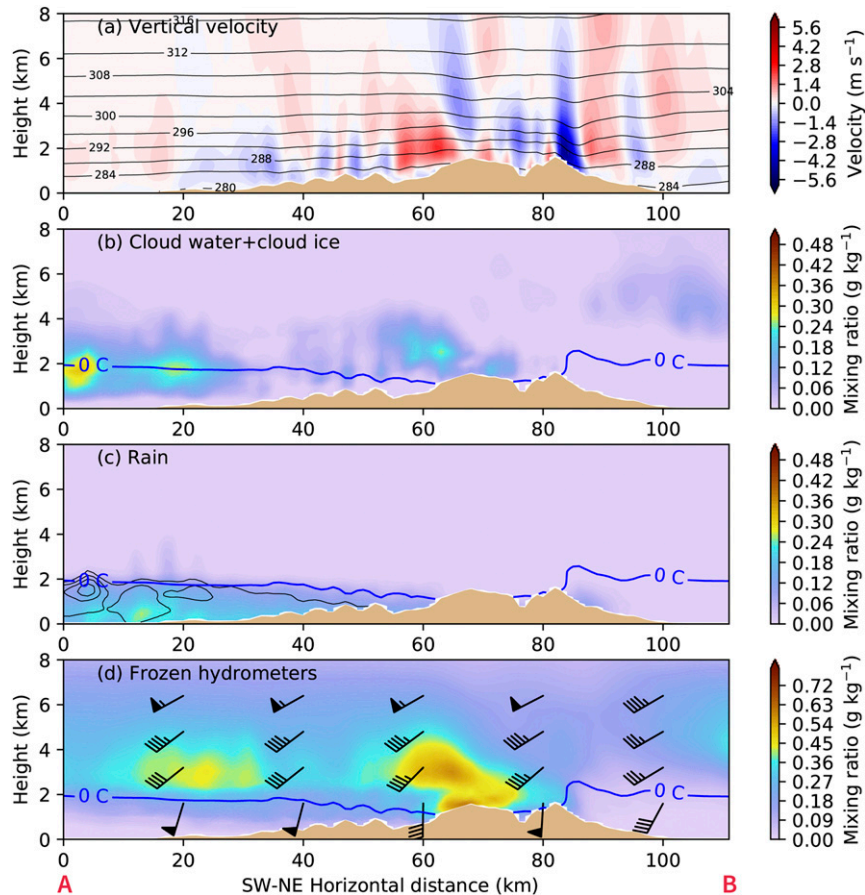
FIG. 8. Composite WRF cross sections for prefrontal sectors taken SW–NE along the red line A–B in Fig. 2. for (a) vertical velocity (m s^{-1}; color contours) and potential temperature (K; black contours); (b) cloud water plus cloud ice mixing ratio (g kg^{-1}) and 0°C isotherm (blue contour); (c) rain mixing ratio (g kg^{-1}), 0°C isotherm (blue contour), and rain number concentration (black contours at every 1000 kg^{-1}, beginning at 2000 kg^{-1}); and (d) frozen hydrometeor mixing ratio mixing ratio (g kg^{-1}), 0°C isotherm (blue contour), and horizontal wind at four vertical levels (kt; barbs).

foothills are generally less than 200 m high. Figures 10c and 11d show that regions of maximum rainwater mixing ratio occurred over the windward slopes, slightly downstream of the regions where the cloud water mixing ratio was the highest. The frozen hydrometeor mixing ratio (Figs. 10d and 11f) was highest over the high terrain, downstream of the maxima in cloud and rainwater on the lower-windward

slopes. The production of frozen hydrometeors (predominantly snow) was tied to the higher-amplitude mountain waves associated with the midlevel barrier-scale crosswinds. The cross section in particular reveals that maxima in cloud water were closely tied to the small-scale mountain waves (Figs. 10a,b), but the broader transition from cloud water to rainwater as illustrated in the cross section
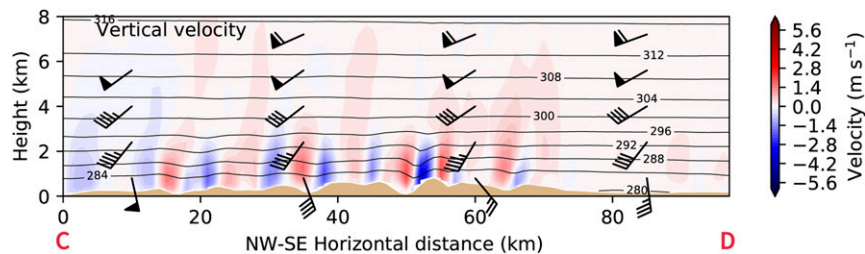

FIG. 9. Composite WRF cross section for prefrontal sectors taken NW–SE along the red line C–D in Fig. 2. All variables are as in Fig. 8a.
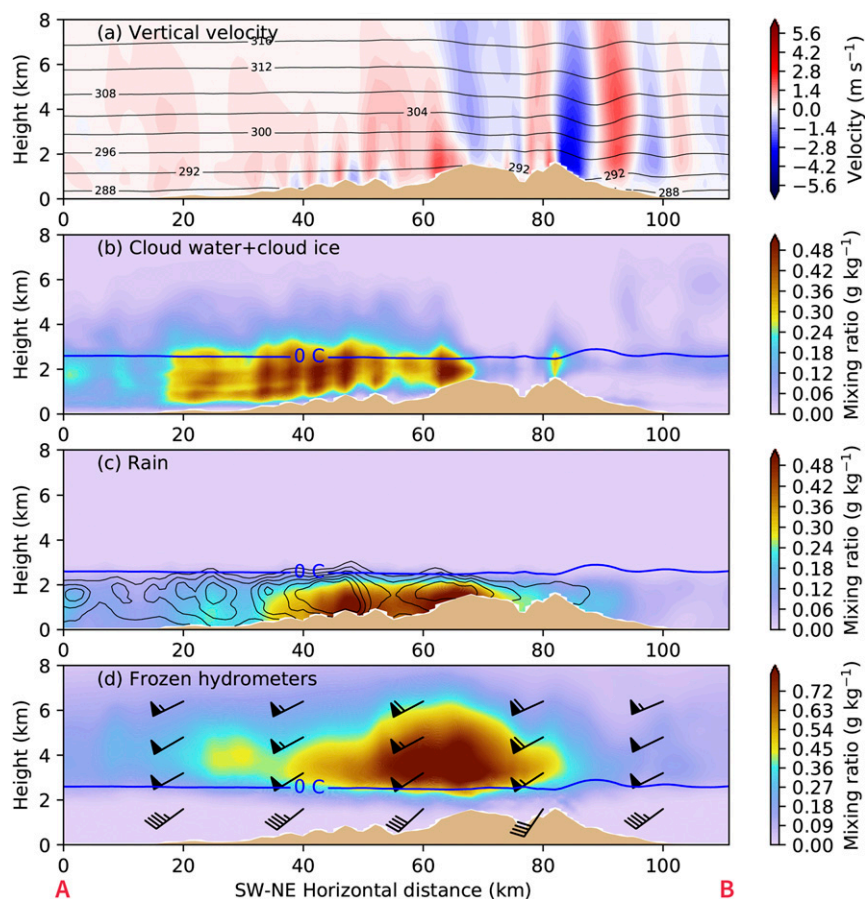
FIG. 10. Composite WRF cross sections for warm sectors taken SW–NE along the red line A–B in Fig. 2. All variables are as in Fig. 8.

(Figs. 10b,c) appears to more broadly be associated with barrier-scale processes along the prevailing wind.

The initial formation of cloud water along the coastal foothills did not result in an immediate increase in precipitation rate at the coast (Fig. 5b). Instead, the model depicts a smooth gradient of increasing precipitation rate up to the windward slopes, with a significant increase in precipitation rate over the lower-windward ridges. Areas of high precipitation rates on the lower-windward slopes tended to be associated with high concentrations of cloud water, suggesting that local enhancements in condensation on windward ridges (i.e., "feeder" clouds) contributed to higher precipitation rates relative to adjacent valleys. The average rain number concentration from the microphysics scheme (black contours in Figs. 8c and 10c) lends further insight into the relative importance of warm processes relative to seeder–feeder. Warm sector rain number concentrations were broadly double to triple that of prefrontal sectors, with the greatest concentrations collocated with the maxima in cloud water concentration.

Disdrometer and gauge observations on the lower-windward slope (the ~500-m elevation Prairie Creek site in Zagrodnik et al. 2018 and Zagrodnik et al. 2019) also indicated a prevalence of large concentrations of small drops in warm sectors, suggesting that the cloud drops are capable of self-collecting to precipitation

size and falling out. Given the tendency of various WRF microphysical schemes to overestimate median drop sizes (D_o) and underestimate the normalized intercept parameter (N_w) in two warm OLYMPEX cases (Conrick et al. 2019a), it is hypothesized that warm precipitation processes are more important than WRF implies. Importantly, these experiments with a bulk microphysical scheme do not directly evaluate how ice-initiated "seeder" particles may accelerate the transition from cloud water to rainwater. While the greatest ice enhancement occurs directly over the barrier in warm sectors and is further advected downstream by >50-kt winds (Fig. 10d), the ice particles formed upstream over the coastal foothills are probably contributing to "seeder–feeder" type enhancement on the windward slopes. However, windward observations in both OLYMPEX (Zagrodnik et al. 2018) and the California foothills (Martner et al. 2008) have shown that rain rates approaching 20 mm h^{-1} can be achieved from largely warm rain processes.

6. Warm rain processes over the coastal foothills

The production of cloud water over the coastal foothills in warm sectors (Fig. 11b) suggests that these foothills are helping facilitate warm rain processes that can produce copious
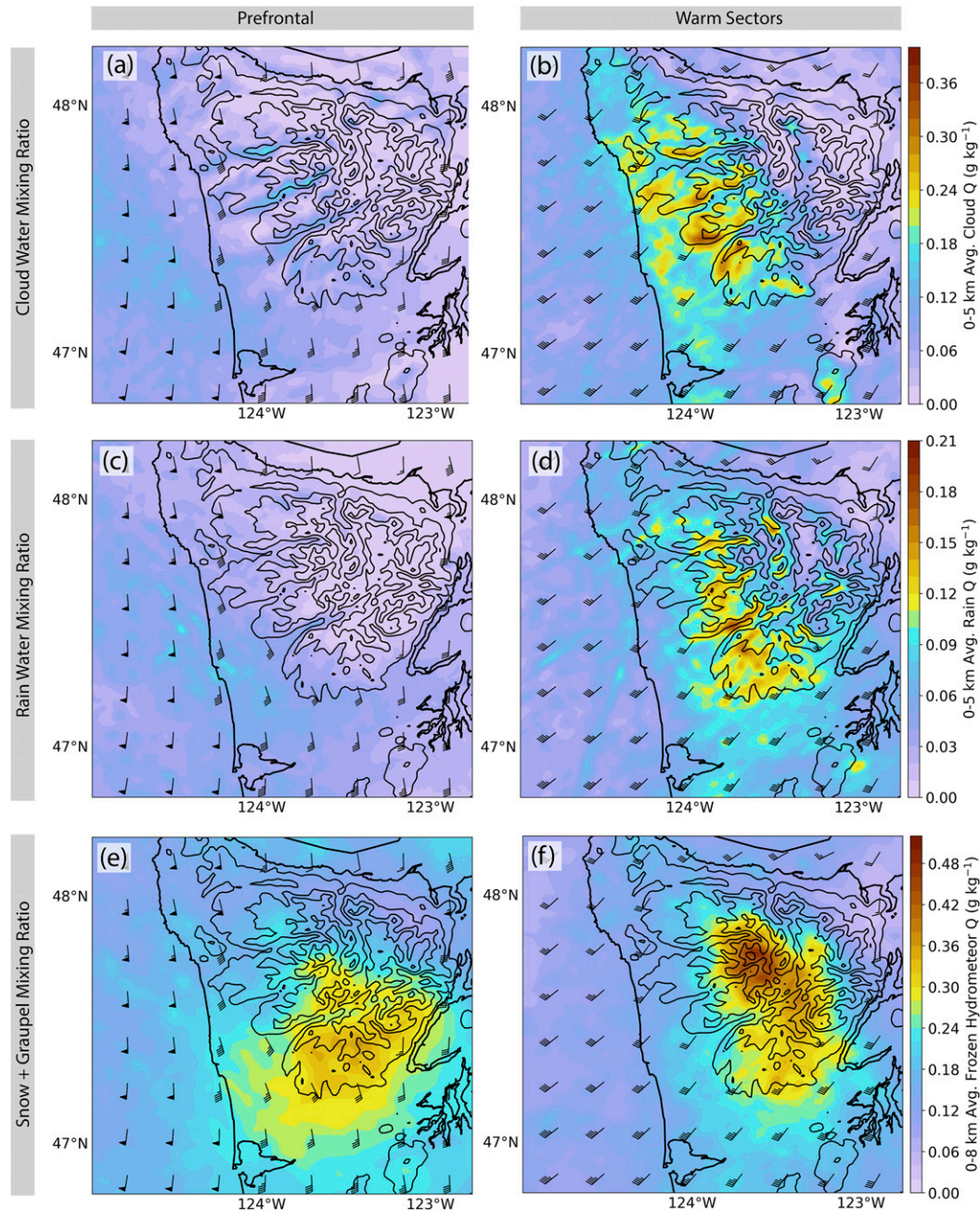
FIG. 11. (a),(b) Composite WRF cloud water mixing ratio (g kg^{-1}) averaged in the 0–5-km layer; (c),(d) composite WRF rain mixing ratio in (g kg^{-1}) averaged in the 0–5-km layer; and (e),(f) composite WRF frozen hydrometeor (snow + graupel) mixing ratio in (g kg^{-1}) averaged in the 0–8-km layer. All panels include 925-hPa wind (kt; barbs). Prefrontal composites are in (a), (c), and (e) and warm sector composites are in (b), (d), and (f).

amounts of rainfall at relatively low elevations (<1000 m) on the windward slopes of the Olympic Mountains. To test this hypothesis, the warm sector WRF simulations were run with the coastal foothills removed. Figure 12 shows the control and modified (foothills removed) terrain. All terrain below 200-m elevation was flattened to 0 m. The artificial terrain edges were initially smoothed over a horizontal distance of 4 km (three grid points). An iterative approach was then applied, during

which six passes were made over the resulting terrain edges, with new edges found after each pass. The resulting terrain in Fig. 11b provides a smooth transition from the Pacific Ocean to high terrain without sacrificing the terrain's natural elevation or the steepness of the primary windward slopes. The coastline location was not modified.

Figures 13 and 14 show the difference between the foothills removed and control runs as a zoomed-in SW–NE cross section
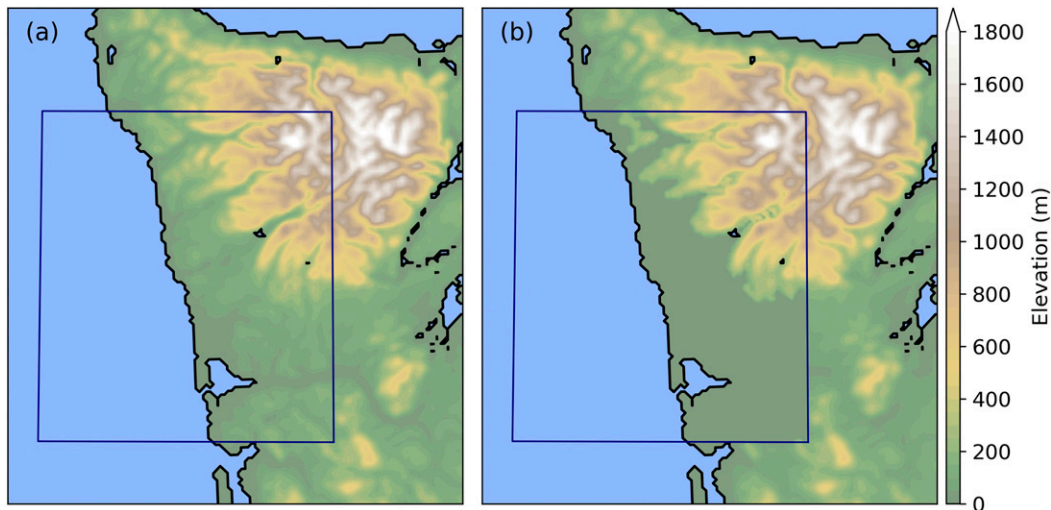
FIG. 12. WRF innermost domain (1.33 km) terrain for the (a) control runs and (b) foothills-removed runs. The box represents the area where terrain below 300 m was flattened to 0 m.

(Fig. 13) and as a map (Fig. 14). The vertical velocity difference in Fig. 13a shows that upward motion is reduced in the leftmost 20 km of the cross section by removing the foothills. The foothills removed run also diminished a wave train that was associated with the transition from ocean to the coastal foothills (faintly visible in Fig. 10a). Of greater interest, a broad region of increased vertical velocity up to 8-km elevation was induced over the windward slopes. The magnitude of the vertical velocity change was relatively small, less than $0.5 \, \text{m s}^{-1}$, but it was enough to cause appreciable changes in the microphysical response to the flow.

Figures 13b–d shows the difference in cloud, rain, and frozen hydrometeor mixing ratios between the foothills removed and control and the modified terrain runs, with Figs. 14a–c showing the corresponding changes in map view. A significant reduction in cloud water mixing ratio (Figs. 13b and 14a) occurred over the flattened foothills with a corresponding increase in cloud water and rainwater over the lower-windward slopes. The percentage of cloud water lost over the flattened area was broadly 30%–40% and locally up to 50%. The frozen hydrometeor mixing ratio Figs. 13c and 14b experienced more modest (10%–20%) changes: a slight decrease over coastal land areas and a slight increase over the middle and higher windward slopes. The cross section (Fig. 14b) suggests that some of the changes to the frozen hydrometeor mixing ratio are the result of changes to the higher-amplitude mountain waves, which may be a secondary effect of the terrain modification.

Figure 14d shows the difference in surface precipitation rate between the two runs. Precipitation rates decreased by 1–$4 \, \text{mm h}^{-1}$ over the coastal foothills and lower-windward slopes and increased by an equivalent magnitude over the higher-windward slopes. The percent change in precipitation was generally in the 20%–40% range in these areas. The total volume of precipitation over the Olympic Peninsula was essentially unchanged. The couplets of positive and negative rain rate (Fig. 14d) and rainwater mixing ratio contours (Fig. 13c) are located downstream of the changes in cloud water mixing

ratio (Figs. 13b, 14a), an indicator of the time needed for cloud drops to grow to precipitation size and fall out. The rain number concentrations also increased within the area of increased rain mixing ratio (Fig. 14c), suggesting warm rain processes were enhanced via the injection of additional cloud water in this region. Since the frozen hydrometeor concentration decreased upstream of the increase in precipitation, there were likely less "seeder" particles available for collecting cloud water. The warm rain processes appear to have more than compensated for this change by converting more cloud water to small raindrops that fell out on the windward slopes.

This simple experiment reveals how condensation upstream of the major windward slopes enables the production of significant precipitation amounts at a relatively low elevation on the windward slopes, well upstream of the higher terrain. It also demonstrates the well-established relationship between complex terrain and microphysical time scales of particle growth, advection, and fallout that are fundamental to linear theories of orographic precipitation (Jiang and Smith 2003; Smith and Barstad 2004). Without the coastal foothills, the initial formation of cloud water was delayed and the precipitation occurred farther downstream. Because the Olympic Mountains are a relatively large barrier, the relevant time scales were still fast enough for the cloud water to be converted to rain and fall out over terrain, rather than being advected over the barrier.

7. Discussion and conclusions

This study builds on previous OLYMPEX observational work (Purnell and Kirshbaum 2018; McMurdie et al. 2018; Zagrodnik et al. 2018, 2019) by using realistic WRF simulations of three prefrontal and three warm sector cases to gain additional insights into the dynamical and microphysical processes that modify precipitation on different scales over a coastal mountain range. Simulated reflectivity and microphysics fields successfully replicated key features from the observations, allowing the model to be
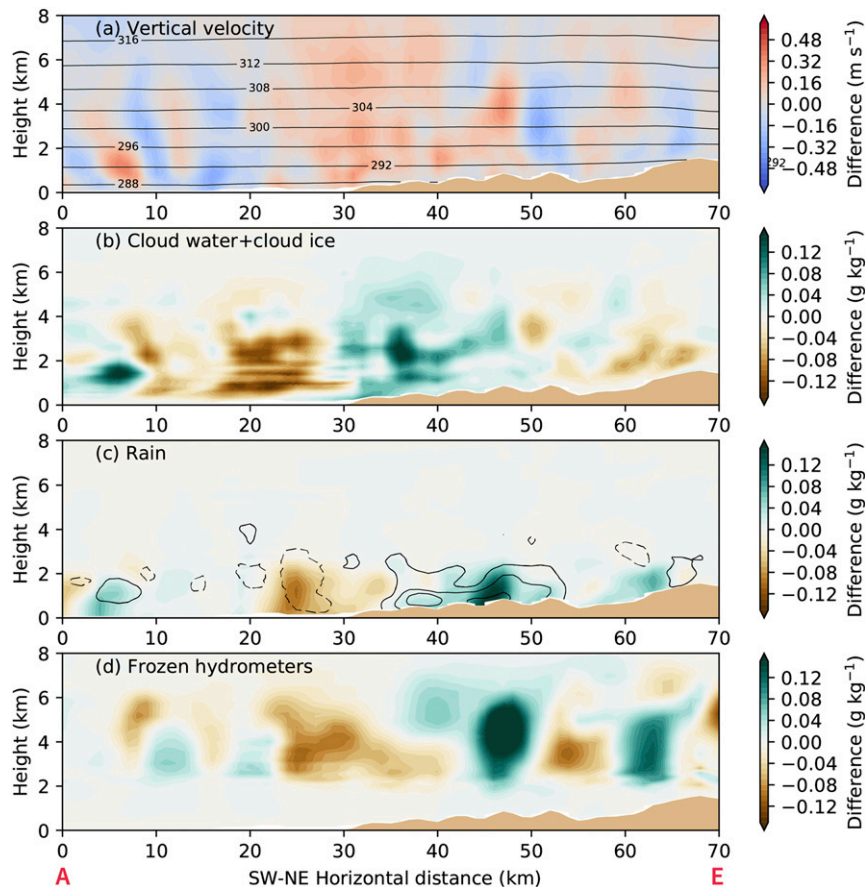
FIG. 13. Difference cross sections SW–NE along the red line A–E in Fig. 2 for (a) vertical velocity (m s^{-1}; color contours), (b) cloud water plus cloud ice mixing ratio (g kg^{-1}), (c) rain mixing ratio (g kg^{-1}) and rain number concentration (black contours at every 1000 kg^{-1}; negative values dashed), and (d) frozen hydrometeor mixing ratio mixing ratio (g kg^{-1}). The potential temperature contours (K) in (a) are from the foothills-removed run. Positive values indicate higher values in the experiment with foothills removed.

confidently used to examine additional aspects of terrain-induced precipitation modification.

a. Key findings

The main finding of this study was that barrier-scale and sub-barrier-scale processes played different roles in producing the observed pattern of precipitation enhancement in prefrontal and warm sectors. In prefrontal sectors, the modest increase in precipitation rate was ultimately driven by ascent over a stably stratified layer upstream of the barrier, enhancing midlevel ice processes. A pronounced pattern of standing mountain waves over the windward slopes was largely inconsequential in enhancing precipitation on the scale of individual ridges. A similar lack of enhancement on windward ridges under low-Froude-number (blocked) conditions was observed by Medina and Houze (2003) and shown in idealized model simulations by Colle (2008). In this study, the modest condensation/deposition and subsequent lee-side evaporation on small-scale ridges occurred on too short of spatial scales to appreciably increase precipitation. In warm sectors, widespread ascent of moist air produced a broad region of

enhanced cloud water across the coast and windward regions. Similar to Minder et al. (2008), the heaviest precipitation rates were closely tied to further ascent along the windward ridges and additional localized condensation. Ice production was less affected by the small-scale windward ridges and was instead enhanced broadly over terrain on the barrier-scale.

A second major finding of this study was the importance of the coastal foothills in producing cloud water upstream of the main topographic barrier. In warm sectors with moist-neutral upstream stability, broad ascent over the coastal region gave the cloud water additional time to self-collect and form into precipitation-sized hydrometeors. Regions of enhanced cloud water were collocated with high rain number concentrations, suggesting that warm rain processes are important in realizing the heavy rain rates at relatively low elevations (500 m and below) on the windward slopes. These model microphysics results are consistent with particle size observations in Zagrodnik et al. (2018), which showed that at ground sites located in the near-coastal lowlands (~50-m Fishery site) and lower-windward slopes (~550-m Prairie Creek site), a significant portion of the rainfall consisted of large quantities of

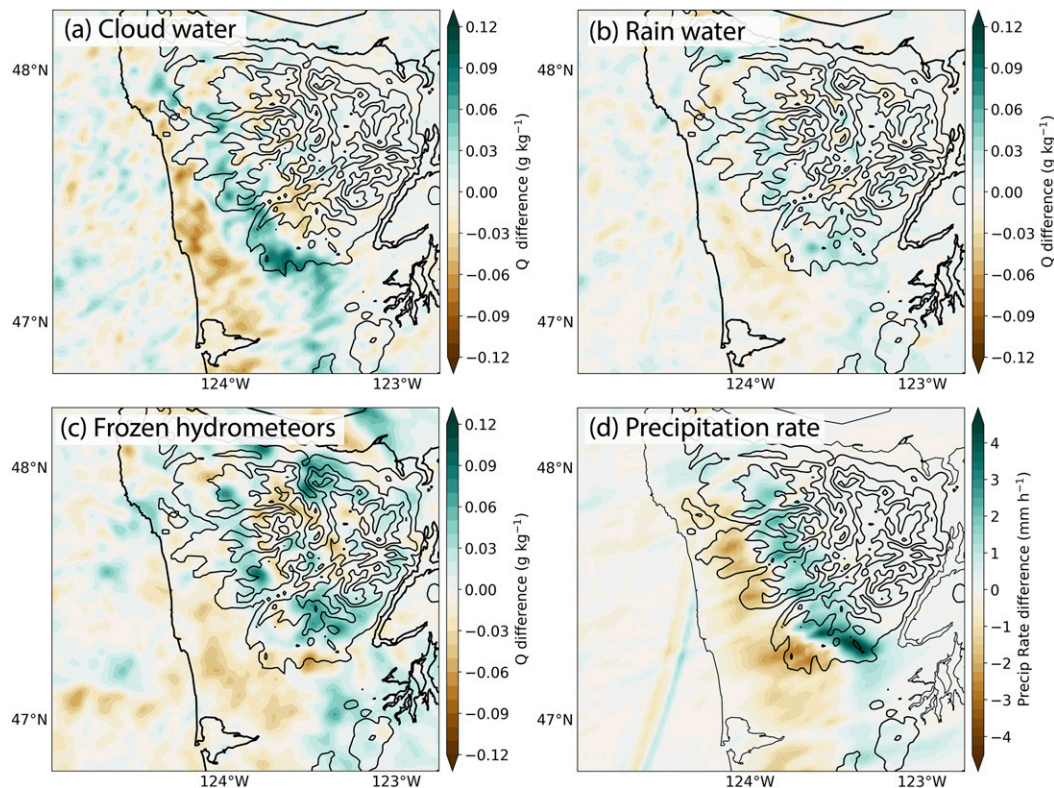FIG. 14. Difference in (a) cloud water mixing ratio (g kg^{-1}) averaged in the 0–5-km layer, (b) rainwater mixing ratio (g kg^{-1}) averaged in the 0–5-km layer, (c) frozen hydrometeor mixing ratio (g kg^{-1}) averaged in the 0–8-km layer, and (d) precipitation rate (mm h^{-1}) in warm sectors between the control and foothills-removed WRF runs. Positive values indicate higher values in the experiment with foothills removed.

small drops. Favorable environmental conditions including moist-neutral static stability, high melting level, and high moisture content assisted in promoting warm rain processes. Collection of cloud water by larger raindrops initiated in the ice layer (seeder–feeder) likely accelerates the fallout at times, but the overwhelming body of observational evidence from OLYMPEX (Zagrodnik et al. 2018; Zagrodnik et al. 2019) suggests that warm rain processes are responsible for a significant portion of the observed precipitation enhancement, especially at lower-windward elevations. Recent model verification studies (Conrick et al. 2019a,b) further point to an underestimation of warm processes and overemphasis on ice processes in WRF microphysics schemes, further lending support to the observational-based warm rain findings.

It is important to emphasize that the Olympic Mountains are a significant mountain range and the storms presented in this study all contain strong synoptic forcing with observed IVT values > 500 kg m^{-1} s^{-1} (Table 3). Weakly forced storms and/or storms passing over smaller hills (e.g., Bergeron 1968) may be more dependent on the seeder–feeder process to accelerate microphysical time scales.

b. Conceptual model

The OLYMPEX field campaign has revealed new insights into the dynamical and microphysical precipitation enhancement processes as midlatitude cyclones pass over a coastal mountain range. Structuring the analysis using a synoptic "storm sector" approach has proven to be a highly effective way of determining the likely modes of precipitation enhancement or lack thereof. The prefrontal and warm sectors are characterized by distinct synoptic-scale environmental conditions (flow, stability, and temperature), which have been shown to exert significant controls over the flow response upon encountering complex terrain.

Figure 15 illustrates many of the key findings of recent OLYMPEX studies (McMurdie et al. 2018; Zagrodnik et al. 2018, 2019) and the present study. This figure builds on the earlier version presented in Zagrodnik et al. (2018). Figure 15a depicts precipitation structures during prefrontal conditions. These periods contain stably stratified low levels, low melting levels, and low-level flow that do not impinge directly on the Olympic Mountains barrier. A moderately deep stratiform cloud layer from the approaching storm is present over the Olympic Mountains with primary precipitation production in the ice layer above the melting level. The ice layer is slightly enhanced upstream of terrain due to lift over the stably stratified lower layer. Relatively small concentrations of larger drops fall from the stratiform cloud with minimal variance in space and time. There is modest enhancement of precipitation on the low- to mid-elevation windward slopes because there is
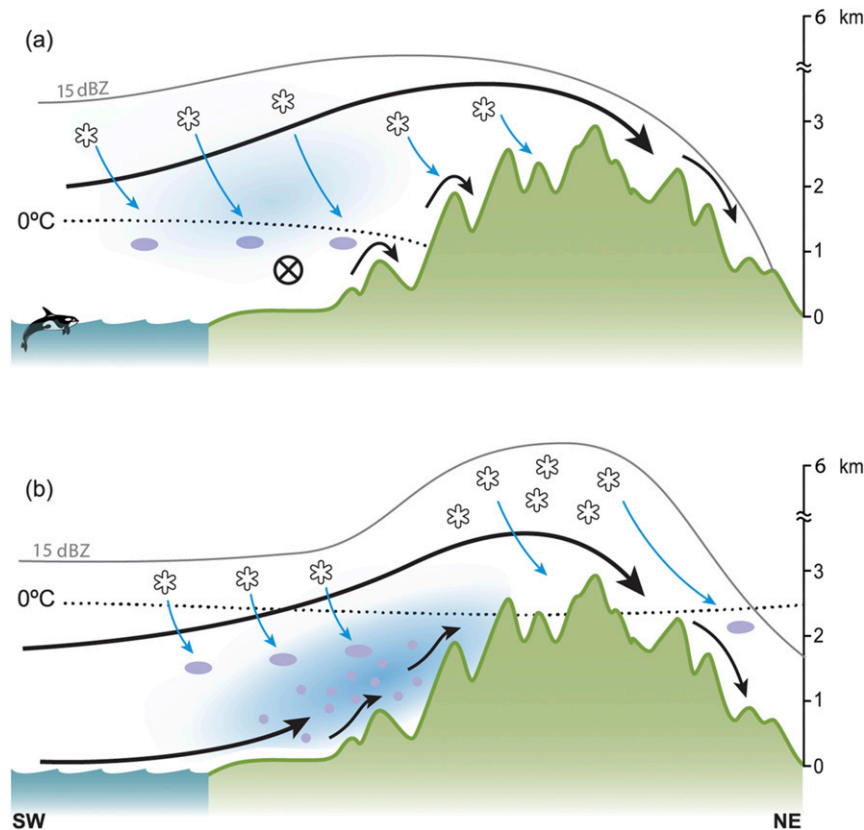
FIG. 15. Conceptual cross-sectional diagrams depicting the two primary modes of precipitation enhancement the Olympic Mountains from southwest to northeast for (a) prefrontal and (b) warm sectors. Large black arrows represent the flow on the scale of the barrier. The ⊗ symbol in (a) represents southeasterly flow perpendicular to the cross section. Small black arrows represent flow on the scale of small-scale (~10 km) ridges. Blue arrows represent frozen hydrometeor trajectories. The gray line represents the average height of the 15-dBZ reflectivity contour (Zagrodnik et al. 2019). The blue shading represents regions of elevated cloud liquid water. Ellipses represent large raindrops formed from melted ice particles. Circles represent small raindrops formed by condensation and collision–coalescence. Snowflakes represent frozen condensate (mostly snow).

minimal generation of cloud water or small raindrops at low elevations. Stationary, small-scale mountain waves over the smaller-scale windward ridges have minimal impact on the overall precipitation pattern. Precipitation diminishes abruptly on the high terrain with a complete rain shadow in the lee.

The bottom panel (Fig. 15b) depicts precipitation structures during warm sectors when heavy precipitation is falling. These periods contain moist-neutral stratification at low levels and high melting levels. The unblocked large-scale flow is directed onshore at both upper and lower levels. The high moisture content of the onshore flow results in the rapid generation of cloud water as soon as the low-level flow begins lifting over the coastal foothills. Large quantities of small drops are formed by condensation and collision–coalescence as the flow continues to ascend moist-neutrally over the lower-elevation windward slopes, especially where lift is locally enhanced along windward ridges. Ice-initiated drops fall in variable quantities upstream of terrain. Directly over terrain the ice layer experiences deep

enhancement. The strong cross-barrier winds advect some of these ice particles downstream to the lee side.

As a whole, OLYMPEX has revealed that the microphysical aspects of precipitation enhancement over the Olympic Mountains depend on a complex mix of warm low-level rain processes and upper-level ice processes. The relative importance of these processes depends in turn on both the sector of the parent synoptic system, the shape of the barrier, and the location relative to the barrier. The heaviest precipitation occurs on the windward slopes where both enhanced warm and ice processes are superimposed during the warm sectors of atmospheric river–type storms.

The warm processes are aided by lift over the coastal foothills, allowing additional time for cloud water to self-collect prior to reaching the windward slopes. The least precipitation enhancement occurs when the warm processes are absent. Warm precipitation processes occur most prominently on the scale of individual ridges, while ice processes are of greater

importance on the barrier scale. Leeside precipitation is often generated by advection of ice processes formed over the barrier (Zagrodnik et al. 2019) and must overcome persistent descent on the downstream side of the higher windward ridges.

Several broad areas of future study can be identified from Fig. 15. The transitional period between prefrontal and warm sectors, the difference between warm and occluded front passages, and the postfrontal sector all deserve additional attention. Additionally, the dynamic and microphysical origins of the deeper ice-layer enhancement over the high terrain is not well understood. Current understanding (McMurdie et al. 2018; Chase et al. 2018), is that riming and aggregation are both enhancing ice processes in a layer concentrated around 4–5-km elevation. Further evaluation of triple-frequency APR-3 retrievals and dual-polarimetric radar data will be required to better understand this interesting feature. These OLYMPEX studies also raise several interesting follow-up questions related to the efficiency of warm microphysical process rates. From a microphysical perspective, it is not clear how a small amount of preexisting, upstream precipitation acts to optimize enhancement processes over terrain, as suggested by Richard et al. (1987) and Purnell and Kirshbaum (2018). Given the strong low level jet velocities associated with atmospheric rivers, shear-induced turbulent cells (Medina et al. 2005; Medina et al. 2007) may also play an unconfirmed role in accelerating collision–coalescence below the melting level. Continued advancements in both in situ and remote sensing–based particle size observation platforms will undoubtedly uncover more details of these processes in future field campaigns.

REFERENCES

Anders, A. M., G. H. Roe, D. R. Durran, and J. R. Minder, 2007: Small-scale spatial gradients in climatological precipitation on the Olympic Peninsula. *J. Hydrometeor.*, **8**, 1068–1081, https://doi.org/10.1175/JHM610.1.

Asencio, N., and J. Stein, 2006: Origins of the reversed flow over the windward Alpine foothills during MAP IOP3 and IOP8. *Quart. J. Roy. Meteor. Soc.*, **132**, 297–316, https://doi.org/10.1256/qj.04.188.

Bergeron, T., 1968: Studies of the orogenic effect on the areal fine structure of rainfall distribution. Meteorology Institute, Uppsala University, Rep. 6, Sweden, 42 pp.

Browning, K. A., F. F. Hill, and C. W. Pardoe, 1974: Structure and mechanism of precipitation and the effect of orography in a wintertime warm sector. *Quart. J. Roy. Meteor. Soc.*, **100**, 309–330, https://doi.org/10.1002/qj.49710042505.

Chase, R. J., and Coauthors, 2018: Evaluation of triple-frequency radar retrieval of snowfall properties using co-incident airborne in situ observations during OLYMPEX. *Geophys. Res. Lett.*, **45**, 5752–5760, https://doi.org/10.1029/2018GL077997.

Colle, B. A., 2008: Two-dimensional idealized simulations of the impact of multiple windward ridges on orographic precipitation. *J. Atmos. Sci.*, **65**, 509–523, https://doi.org/10.1175/2007JAS2305.1.

Conrick, R., and C. F. Mass, 2019a: An evaluation of simulated precipitation characteristics during OLYMPEX. *J. Hydrometeor.*, **20**, 1147–1164, https://doi.org/10.1175/JHM-D-18-0144.1.

——, and ——, 2019b: Evaluating simulated microphysics during OLYMPEX using GPM satellite observations. *J. Atmos. Sci.*, **76**, 1093–1105, https://doi.org/10.1175/JAS-D-18-0271.1.

Durden, S. L., and S. Tanelli, 2018: GPM ground validation Airborne Precipitation Radar 3rd Generation (APR-3) OLYMPEX, version 2. NASA Global Hydrology Center DAAC, accessed 8 May 2018, https://doi.org/10.5067/GPMGV/OLYMPEX/APR3/DATA201.

Durran, D. R., and J. B. Klemp, 1982: On the effects of moisture on the Brunt–Väisälä frequency. *J. Atmos. Sci.*, **39**, 2152–2158, https://doi.org/10.1175/1520-0469(1982)039<2152:OTEOMO>2.0.CO;2.

Garvert, M. F., B. Smull, and C. Mass, 2007: Multiscale mountain waves influencing a major orographic precipitation event. *J. Atmos. Sci.*, **64**, 711–737, https://doi.org/10.1175/JAS3876.1.

Grell, G. A., and S. R. Freitas, 2014: A scale and aerosol aware stochastic convective parameterization for weather and air quality modeling. *Atmos. Chem. Phys.*, **14**, 5233–5250, https://doi.org/10.5194/acp-14-5233-2014.

Hill, F. F., K. A. Browning, and M. J. Bader, 1981: Radar and raingauge observations of orographic rain over South Wales. *Quart. J. Roy. Meteor. Soc.*, **107**, 643–670, https://doi.org/10.1002/qj.49710745312.

Hong, S.-Y., Y. Noh, and J. Dudhia, 2006: A new vertical diffusion package with an explicit treatment of entrainment processes. *Mon. Wea. Rev.*, **134**, 2318–2341, https://doi.org/10.1175/MWR3199.1.

Horel, J., and Coauthors, 2002: Mesowest: Cooperative mesonets in the western United States. *Bull. Amer. Meteor. Soc.*, **83**, 211–225, https://doi.org/10.1175/1520-0477(2002)083<0211:MCMITW>2.3.CO;2.

Houze, R. A., C. N. James, and S. Medina, 2001: Radar observations of precipitation and airflow on the Mediterranean side of the Alps: Autumn 1998 and 1999. *Quart. J. Roy. Meteor. Soc.*, **127**, 2537–2558, https://doi.org/10.1002/qj.49712757804.

——, and Coauthors, 2017: The Olympic Mountains Experiment (OLYMPEX). *Bull. Amer. Meteor. Soc.*, **98**, 2167–2188, https://doi.org/10.1175/BAMS-D-16-0182.1.

Iacono, M. J., J. S. Delamere, E. J. Mlawer, M. W. Shephard, S. A. Clough, and W. D. Collins, 2008: Radiative forcing by long-lived greenhouse gases: Calculations with the AER radiative transfer models. *J. Geophys. Res.*, **113**, D13103, https://doi.org/10.1029/2008JD009944.

James, C. N., and R. A. Houze, 2005: Modification of precipitation by coastal orography in storms crossing Northern California. *Mon. Wea. Rev.*, **133**, 3110–3131, https://doi.org/10.1175/MWR3019.1.

Jankov, I., J.-W. Bao, P. J. Neiman, P. J. Schultz, H. Yuan, and A. B. White, 2009: Evaluation and comparison of microphysical algorithms in ARW-WRF Model simulations of atmospheric river events affecting the California coast. *J. Hydrometeor.*, **10**, 847–870, https://doi.org/10.1175/2009JHM1059.1.

Jiang, Q., and R. B. Smith, 2003: Cloud timescales and orographic precipitation. *J. Atmos. Sci.*, **60**, 1543–1559, https://doi.org/10.1175/2995.1.

Kingsmill, D. E., P. J. Neiman, F. M. Ralph, and A. B. White, 2006: Synoptic and topographic variability of Northern California precipitation characteristics in landfalling winter storms observed during CALJET. *Mon. Wea. Rev.*, **134**, 2072–2094, https://doi.org/10.1175/MWR3166.1.

Martner, B. E., S. E. Yuter, A. B. White, S. Y. Matrosov, D. E. Kingsmill, and F. M. Ralph, 2008: Raindrop size distributions and rain characteristics in California coastal rainfall for periods with and without a radar bright band. *J. Hydrometeor.*, **9**, 408–425, https://doi.org/10.1175/2007JHM924.1.

Massmann, A. K., J. R. Minder, R. D. Garreaud, D. E. Kingsmill, R. A. Valenzuela, A. Montecinos, S. L. Fults, and J. R. Snider, 2017: The Chilean coastal orographic precipitation experiment: Observing the influence of microphysical rain regimes on coastal orographic precipitation. *J. Hydrometeor.*, **18**, 2723–2743, https://doi.org/10.1175/JHM-D-17-0005.1.

McMurdie, L. A., A. K. Rowe, R. A. Houze, S. R. Brodzik, J. P. Zagrodnik, and T. M. Schuldt, 2018: Terrain-enhanced precipitation processes above the melting layer: Results from OLYMPEX. *J. Geophys. Res. Atmos.*, **123**, 12 194–12 209, https://doi.org/10.1029/2018JD029161.

Medina, S., and R. A. Houze Jr., 2003: Air motions and precipitation growth in Alpine storms. *Quart. J. Roy. Meteor. Soc.*, **129**, 345–371, https://doi.org/10.1256/qj.02.13.

——, B. F. Small, R. A. Houze, and M. Steiner, 2005: Cross-barrier flow during orographic precipitation events: Results from MAP and IMPROVE. *J. Atmos. Sci.*, **62**, 3580–3598, https://doi.org/10.1175/JAS3554.1.

——, E. Sukovich, and R. A. Houze, 2007: Vertical structures of precipitation in cyclones crossing the Oregon Cascades. *Mon. Wea. Rev.*, **135**, 3565–3586, https://doi.org/10.1175/MWR3470.1.

Minder, J. R., D. R. Durran, G. H. Roe, and A. M. Anders, 2008: The climatology of small-scale orographic precipitation over the Olympic Mountains: Patterns and processes. *Quart. J. Roy. Meteor. Soc.*, **134**, 817–839, https://doi.org/10.1002/qj.258.

Nash, J., and K. A. Browning, 1977: Structure of the lower atmosphere associated with heavy falls of orographic rain in South Wales. Meteorological Office Radar Research Laboratory Rep. 7, 26 pp.

Niu, G.-Y., and Coauthors, 2011: The community Noah land surface model with Multiparameterization Options (Noah-MP): 1. Model description and evaluation with local-scale measurements. *J. Geophys. Res.*, **116**, D12109, https://doi.org/10.1029/2010JD015139.

Petersen, W. A., D. Wolff, J. Wang, and A. Tokay, 2017a: GPM ground validation Met One rain gauge pairs OLYMPEX. NASA Global Hydrology Center DAAC [Subset used: All sites, November–December 2015], accessed 23 April 2018, https://doi.org/10.5067/GPMGV/OLYMPEX/GAUGES/DATA201.

——, A. Tokay, and P. N. Gatlin, 2017b: GPM ground validation Pluvio precipitation gauges OLYMPEX. NASA Global Hydrology Center DAAC [Subset used: Wynoochee site, November–December 2015], accessed 1 March 2019, https://doi.org/10.5067/GPMGV/OLYMPEX/PLUVIO/DATA301.

Purnell, D. J., and D. J. Kirshbaum, 2018: Synoptic control over orographic precipitation distributions during the Olympics Mountains Experiment (OLYMPEX). *Mon. Wea. Rev.*, **146**, 1023–1044, https://doi.org/10.1175/MWR-D-17-0267.1.

Richard, E., N. Chaumerliac, J. F. Mahfouf, and E. C. Nickerson, 1987: Numerical simulation of orographic enhancement of rain with a mesoscale model. *J. Climate Appl. Meteor.*, **26**, 661–669, https://doi.org/10.1175/1520-0450(1987)026<0661:NSOOEO>2.0.CO;2.

Skamarock, C., and Coauthors, 2008: A description of the Advanced Research WRF version 3. NCAR Tech. Note NCAR/TN-475+STR, 113 pp., https://doi.org/10.5065/D68S4MVH.

Smith, R. B., and I. Barstad, 2004: A linear theory of orographic precipitation. *J. Atmos. Sci.*, **61**, 1377–1391, https://doi.org/10.1175/1520-0469(2004)061<1377:ALTOOP>2.0.CO;2.

Steiner, M., O. Bousquet, R. A. Houze, B. F. Smull, and M. Mancini, 2003: Airflow within major Alpine river valleys under heavy rainfall. *Quart. J. Roy. Meteor. Soc.*, **129**, 411–431, https://doi.org/10.1256/qj.02.08.

Thériault, J., and Coauthors, 2012: A case study of processes impacting precipitation phase and intensity during the Vancouver 2010 Winter Olympics. *Wea. Forecasting*, **27**, 1301–1325, https://doi.org/10.1175/WAF-D-11-00114.1.

Thompson, G., P. R. Field, R. M. Rasmussen, and W. D. Hall, 2008: Explicit forecasts of winter precipitation using an improved bulk microphysics scheme. Part II: Implementation of a new snow parameterization. *Mon. Wea. Rev.*, **136**, 5095–5115, https://doi.org/10.1175/2008MWR2387.1.

White, A. B., P. J. Neiman, F. M. Ralph, D. E. Kingsmill, and P. O. G. Persson, 2003: Coastal orographic rainfall processes observed by radar during the California Land-Falling Jets Experiment. *J. Hydrometeor.*, **4**, 264–282, https://doi.org/10.1175/1525-7541(2003)4<264:CORPOB>2.0.CO;2.

Zagrodnik, J. P., L. A. McMurdie, and R. A. Houze, 2018: Stratiform precipitation processes in cyclones passing over a coastal mountain range. *J. Atmos. Sci.*, **75**, 983–1004, https://doi.org/10.1175/JAS-D-17-0168.1.

——, ——, ——, and S. Tanelli, 2019: Vertical structure and microphysical characteristics of frontal systems passing over a three-dimensional coastal mountain range. *J. Atmos. Sci.*, **76**, 1521–1546, https://doi.org/10.1175/JAS-D-18-0279.1.